MNRAS 000, 1–12 (2022) Preprint 3 May 2023 Compiled using MNRAS LATEX style file v3.0

Comparison of a pebbles-based model with the observed evolution of the water and carbon dioxide outgassing of comet 67P/Churyumov-Gerasimenko

Mauro Ciarniello,[1]⋆ M. Fulle,[2] F. Tosi,[1] S. Mottola,[3] F. Capaccioni,[1] D. Bockelée-Morvan,[4] A. Longobardo,[1] A. Raponi,[1] G. Filacchione,[1] G. Rinaldi,[1] A. Rotundi,[5,1] M. C. De Sanctis,[1] M. Formisano,[1] and G. Magni[1]

[1]*IAPS-INAF, Istituto di Astrofisica e Planetologia Spaziali, via del Fosso del Cavaliere, 100, 00133, Rome, Italy*
[2]*INAF - Osservatorio Astronomico, Trieste, Italy*
[3]*Institute for Planetary Research, German Aerospace Center (DLR), Berlin, Germany*
[4]*LESIA, Observatory of Paris, PSL University, CNRS, Sorbonne University, University of Paris, Meudon, France*
[5]*Università degli Studi di Napoli Parthenope, Dip. di Scienze e Tecnologie, Naples, Italy*

Accepted XXX. Received YYY; in original form ZZZ

ABSTRACT

The Rosetta mission escorted comet 67P/Churyumov-Gerasimenko for approximately two years including the perihelion passage (1.24 au, August 2015), allowing us to monitor the seasonal evolution of the water and carbon dioxide loss rates. Here, we model 67P/Churyumov-Gerasimenko water and carbon dioxide production as measured by the Rosina experiment during the entire escort phase by applying the WEB (Water-ice-Enriched Block) model, namely a structural and activity model for a nucleus made of pebbles. Furthermore, we compare the surface temperature distribution inferred by VIRTIS-M observations in August 2014 (≈3.5 au inbound, northern summer) with the expected temperatures from our simulations in the nucleus' northern hemisphere, investigating the relevance of self-illumination effects in the comet "neck" and assessing the active area extent during the northern summer. Our simulations imply that: 1) water production at perihelion is mostly from the dehydration of water-poor pebbles, continuously exposed by CO_2-driven erosion; 2) at large heliocentric distances outbound the water loss rate is dominated by the self-cleaning of fallout deposits; 3) the outbound steep decrease of the water production curve with heliocentric distance results from the progressive reduction of the nucleus water-active area, as predicted by the proposed model; 4) in August 2014 the water production is dominated by distributed sources, originating in the active "neck"; 5) distributed sources originating in water-ice-rich exposures dominate the water production approximately up to the inbound equinox; 6) the time evolution of the CO_2 loss rate during the Rosetta escort phase is consistent with the WEB model.

Key words: comets: general – comets: individual: 67P/Churyumov-Gerasimenko – methods: analytical – methods: numerical – space vehicles

1 INTRODUCTION

Before ESA's Giotto mission to comet 1P/Halley, the thermophysical models of cometary nuclei assumed that pure water ice was exposed on the nucleus surface (Delsemme 1982). The water-vapor loss rates computed according to the early measurements of nuclei's cross sections often resulted in values much larger than the observed ones, so that the concept of active area fraction was introduced, e.g. close to 8% in case of 67P/Churyumov-Gerasimenko (hereafter 67P) (Lis et al. 2019). After the Giotto mission, which found a nucleus much darker than expected, most of the subsequent thermophysical models of cometary nuclei were based on the assumption of a desiccated crust, mantling an interior richer in water ice (e.g. Keller et al. 2015; Davidsson et al. 2022). This assumption required additional free parameters, as the thickness of the crust and the nucleus active area fraction (Hu et al. 2017).

Crust-based models, however, cannot explain the presence of dust in the coma, because the gas pressures at the nucleus surface are always lower than 0.1 Pa (Pajola et al. 2017b), i.e. lower than the tensile strengths bonding sub-cm dust particles to the nucleus (Skorov & Blum 2012; Gundlach et al. 2015), unless particular crust properties are assumed, e.g. a meter-thick mantle depleted of super-volatiles and with pores of sizes ≤ 1 mm (Bouziani & Jewitt 2022), however inconsistent with the ejection of dm-sized chunks from Jupiter Family Comets (Kelley et al. 2015; Fulle et al. 2016; Ott et al. 2017; Gundlach et al. 2020; Ciarniello et al. 2022; Lemos et al. 2023), or, for the case of 67P, ad-hoc spatial variability of the dust mantle thickness coupled with the comet specific illumination conditions (Skorov et al. 2020). Also, the observed evolution of the 67P nucleus color excludes the presence of a desiccated crust (Ciarniello et al. 2022). Models based on a crust (e.g. Davidsson et al. 2022), although con-

⋆ E-mail: mauro.ciarniello@inaf.it (MC)

sistent with the measured dust deposition (Cambianica et al. 2020), are inconsistent with the measured 67P nucleus erosion (Cambianica et al. 2020), which implies values of the nucleus refractory-to-water-ice mass ratio δ orders of magnitude larger than those provided by crust models, which thus seem not being able to constrain δ reliably. Depending on the model, the mantle thickness ranges from a few tens of μm (Keller et al. 2015) to a meter (Bouziani & Jewitt 2022) according to the fit of the different observations.

Recently, a nucleus thermophysical model consistent both with dust ejection and with all available data of cometary dust (Güttler et al. 2019) has been developed (Fulle et al. 2020), assuming the presence of Water-ice-Enriched Blocks (WEBs) in pebble-made comets and here named WEB model (Ciarniello et al. 2022). It shows that the only parameter-free approach to overcome the cohesion bottleneck between dust and nucleus is the sublimation of water-ice occurring inside the particles composing the nucleus pebbles, because only there all the pores are small enough to force the gas pressure to reach values of many Pa, thus providing steep pressure gradients at the pebble surface. Rosetta data provide a ratio $\chi \approx 10^5$ between the sizes of the pebbles and that of the grains composing the dust particles (Güttler et al. 2019). In this respect, experiments based on $\chi < 10$ (Kossacki et al. 2023) cannot measure the pressure gradient at the pebble surface.

The WEB model fits most collected data at 67P (Fulle et al. 2020; Fulle 2021). Furthermore, basing on the assumption that comets are formed by two classes of pebbles (Ciarniello et al. 2022), namely water-ice-rich ($\delta_r \approx 2$, O'Rourke et al. 2020) and water-ice-poor ($\delta_p \approx 50$, Fulle 2021, the actual uncertainty of this δ-value is discussed in Section 4.1), with different deuterium-to-hydrogen ratio — $D/H_r = 1.56 \times 10^{-4}$ (Vienna Standard Mean Ocean Water de Laeter et al. 2003) and $D/H_p = 5.3 \pm 0.7 \times 10^{-4}$ (Altwegg et al. 2015), respectively — the WEB model predicts the anti-correlation between the deuterium-to-hydrogen ratio and the hyperactivity of comets (Lis et al. 2019; Fulle 2021). The updated D/H value of 67P and its invariability within the measurement uncertainties with heliocentric distance and level of activity (Müller et al. 2022) perfectly matches the predictions in case of 67P negligible water distributed sources at perihelion (Fulle 2021). The WEB model confirms that nuclei of comets are composed of cm-sized pebbles (Blum et al. 2017), which are inhomogeneous clusters of porous dust particles, i.e. porous agglomerates of rocks (Brownlee et al. 2006) and ice-enveloped dust grains (Güttler et al. 2019; Fulle et al. 2020).

Here we show that the WEB model also fits with good accuracy the observed temporal evolution of 67P water and carbon dioxide loss rates (Läuter et al. 2020) across the Rosetta escort phase, in a consistent picture with the above-mentioned previous findings and allowing us to characterise the processes concurring to water production. In particular, we show that around perihelion, the water loss rate is dominated by dehydration of water-bearing pebbles exposed by CO_2-driven erosion occurring over part of the surface (Gundlach et al. 2020), while after the outbund equinox the water production is driven by self-cleaning of fallout material (Pajola et al. 2017a). Also, we find that distributed sources dominate water production approximately up to the inbound equinox.

2 WATER ACTIVITY MODEL

In this section we provide a brief summary of the WEB model (Fulle et al. 2020; Ciarniello et al. 2022). For brevity we do not report a full description of the model equations, which the interested reader can find in the dedicated paper. Nonetheless, we provide here a reference for key modelled quantities involved in the computation of 67P water production rate.

At each heliocentric distance r_h and solar zenithal angle θ determining the incident solar flux F, the WEB model (Fulle et al. 2020) is defined by five analytical equations fixing (i) the average temperature T of the sunlit pebbles, which depends on F; (ii) the water-vapor pressure P and (iii) the gas flux q from the nucleus surface; (iv) the heat conductivity λ_s; and (v) the temperature gradient ∇T at depths of a few cm. All these quantities depend on T. A nucleus is active if the gas pressure P overcomes the tensile strength S bonding dust particles to the nucleus surface (Skorov & Blum 2012). If this condition is not met, dust ejection is quenched, and the water ice sublimation builds up an insulating crust finally stopping the activity in e.g. half-an-hour at 67P perihelion (Section 4.1). According to the WEB model, dust ejection is possible only if $T \geq 205$ K, thus representing the activity onset temperature. In Fig. 1 we report the expected surface temperature as a function of the solar flux, while in Fig. 2 the gas flux q as a function of T. The WEB model is defined at thermal equilibrium (Fulle et al. 2020), so that it cannot provide the transition from steady activity at T≥205 K to inactivity due to the presence of a crust at T<205 K. The activity onset temperature is reached for an incident solar flux of 96 $\mathrm{Wm^{-2}}$, corresponding to a heliocentric distance of approximately 3.8 au at normal incidence, while around perihelion, the maximum average temperature of pebbles exposed to sunlight is approximately 275 K.

The above quantities allow us to compute also the dehydration rate D (the thickness dehydrated per unit time because of water ice sublimation, proportional to $1 + \delta$, Eq. 1a), and the water-driven erosion rate E (the thickness eroded per unit time by dust ejection). Since the dust volume distribution is dominated by the largest particles (Güttler et al. 2019; Fulle et al. 2020), the erosion rate is computed as the ratio of the size of the largest ejected particle s_M and the timescale of heat conduction at depth s_M. The size of the largest ejected particle is an output of the model and corresponds to the maximum depth at which the water vapour pressure overcomes the tensile strength of the dust aggregates. This depends on the temperature profile with depth, which in turn is univocally determined by the surface temperature T. Given this, the size of the largest ejected particle can be expressed as $s_M(T)$. The timescale of heat conduction at depth s_M is given by $\rho_d c_p s_M^2/\lambda_s(s_M)$, where $\lambda_s(s_M)$ is the heat conductivity at depth s_M, $\rho_d \approx 800$ kg m^{-3} is the average dust bulk density (Fulle et al. 2017) and $c_p \approx 10^3$ J kg^{-1}K^{-1} is the heat capacity of the pebbles (Blum et al. 2017). As such, the erosion rate E is only a function of T and does not depend on δ (see eq. 1b and Fig. 2). By comparing eqs. 1a and 1b, we can define the refractory-to-water-ice mass ratio for which $E(T) = D(T)$ at each temperature. We refer to this value as δ_{MAX}, being the maximum refractory-to-water-ice mass ratio at a given T for which the dehydration rate is not larger than the erosion rate ($D(T) \leq E(T)$) (Eq. 1c, Fig. 2).

$$D(T) = \frac{(1+\delta)q(T)}{\rho_n}, \tag{1a}$$

where $\rho_n = 538$ kgm^{-3} is the nucleus density (Pätzold et al. 2019),

$$E(T) = \frac{\lambda_s(s_M)}{\rho_d c_p s_M(T)}, \tag{1b}$$

$$\delta_{MAX}(T) = \frac{E(T)\rho_n}{q(T)} - 1. \tag{1c}$$

Water-driven activity can be sustained if $D < E$, implying that the surface pebbles are eroded by dust ejection before being dehydrated, and exposing underlying water-ice-bearing pebbles. Conversely, if

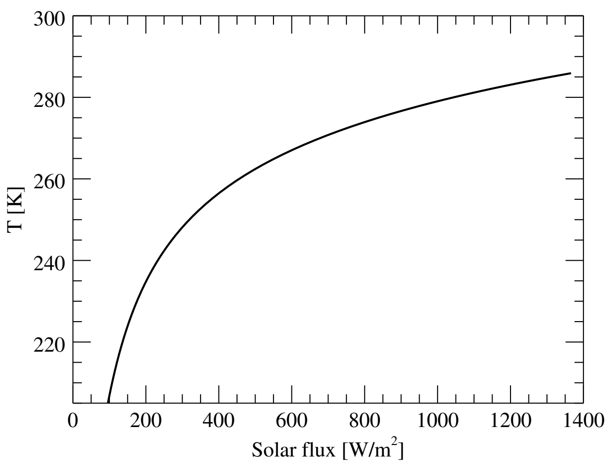

Figure 1. Average temperature T of the sunlit pebbles as a function of the incident solar flux F at the nucleus surface (Fulle et al. 2020). Average temperatures $T < 205$ K make a comet water-inactive, so they are not shown here.

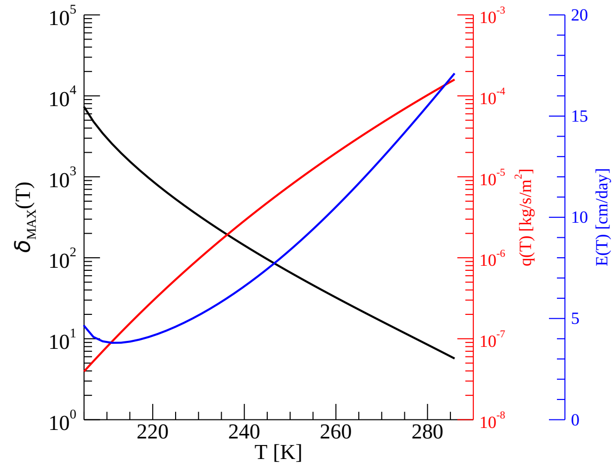

Figure 2. Water vapor flux $q(T)$ (red curve), erosion rate $E(T)$ (blue curve), and refractory-to-water-ice mass ratio $\delta_{MAX}(T)$ (black curve) for which the erosion rate is equal to the dehydration rate ($D = E$), as functions of the average temperature T of the sunlit pebbles (Fulle et al. 2020). $T < 205$ K makes a comet water-inactive.

$D > E$, the surface pebbles get dehydrated before dust is ejected, developing an insulating layer which dumps further activity (Fulle et al. 2020), unless additional erosion mechanisms takes place. At temperatures just above $T = 205$ K ($\delta_{MAX} \approx 0.7 \times 10^4$, Fig. 2), $D < E$ for most possible δ-values (Fulle 2021), so that 67P activity is driven by sublimation of residual water-ice also in dust deposits by the so-called self-cleaning process (Pajola et al. 2017b). Around perihelion, $D < E$ occurs only in exposed WEBs for which $\delta \approx 2 < \delta_{MAX} \approx 5$ (Fulle 2021; Ciarniello et al. 2022), where the erosion is driven by water-ice sublimation. However, around perihelion, the overall nucleus erosion is dominated by CO_2-driven activity (Gundlach et al. 2020; Ciarniello et al. 2022), which exposes to a continuous dehydration also the rest of the nucleus surface, which is composed of water-poor pebbles of $\delta \approx 50$ where $D > E$. In our computation we assume that CO_2-driven erosion is fast enough to expose new pebbles as the old ones get dehydrated (Fulle 2021), thus providing the condition for a potentially all active surface. Following from this assumption, all the portion of the surface at the same temperature $T > 205$ K provide the same water-vapor flux q (Fig. 2) also around perihelion.

3 WATER LOSS RATE COMPUTATION: FROM ILLUMINATION MAPS TO THE MODELED WATER LOSS RATE CURVE

To compute the water loss rate with the WEB model we assume that all the surface elements with a temperature larger than 205 K are active (potentially all-active surface). The energetic input in each position is derived by taking advantage of the illumination maps by Beth et al. (2017). These are computed as a function of the subsolar point position at 1° steps of subsolar longitude (0°–360°) and latitude (-52°–52°) by using the shape model `CSHP_DV_130_01_LORES_OBJ.OBJ` (104192 facets), and provide the cosine of the angle θ_ι between the Sun direction and the normal to the ι-th facet. This quantity is used to calculate the Solar flux $F_\iota = J cos(\theta_\iota)/r_h^2$, with r_h being the comet heliocentric distance and J the Solar irradiance at 1 au. From F_ι we compute the temperature of the surface pebbles at each facet (T_ι) through the relation shown in Fig. 1. The total water loss rate Q_{tot} at each position along the orbit is computed as $Q_{tot} = \sum_\iota q_\iota(T_\iota)\Delta A_\iota$ providing the sum of the water flux from each facet $q_\iota(T_\iota)$ times the facet area ΔA_ι. To account for the water loss rate variability over one comet rotation the computation is repeated over 360 subsolar longitude steps, for each position along the orbit. The computed water vapor loss rate curve is reported in Fig. 3, compared to the measured water loss rate derived from Läuter et al. (2020), and the average value of the nucleus area where $T > 205$ K.

4 WATER LOSS RATE: MEASURED VS. MODELED

Läuter et al. (2020) report the water loss rate for comet 67P during the escort phase of the Rosetta mission, from 2014 August 1 (heliocentric distance of 3.63 au inbound) to 2016 September 5 (3.70 au outbound), as inferred from measurements of the COPS (COmet Pressure Sensor) and DFMS (Double Focusing Mass Spectrometer) sensors of the ROSINA (Rosetta Orbiter Spectrometer for Ion and Neutral Analysis, Balsiger et al. 2007)) instrument (Fig. 3). Their estimation of the water production temporal evolution is generally in good agreement with results from different authors (Hansen et al. 2016; Biver et al. 2019; Combi et al. 2020), and we refer to such water loss rate curve to carry out the comparison with our computation. According to Läuter et al. (2020), the water production reaches its peak ($Q_{MAX} = [1.85 \pm 0.03] \times 10^{28}$ molecules/s) approximately three weeks after perihelion, whereas the WEB model, assuming thermal equilibrium, predicts a peak at perihelion, a difference however not appreciable in Fig. 3, due to the uncertainties of the measurements after perihelion and the diurnal oscillations of the computed water loss rate (grey band in Fig. 3). The water loss rate reduction with heliocentric distance occurs in an asymmetric fashion between the inbound and outbound legs. In the latter case, the water production is characterised by a steep drop at large heliocentric distances ($[4.1 \pm 1.3] \times 10^{24}$ molecules/s at ≈ 3.6 au), while, along the inbound orbit at $\approx 3.6 - 3.1$ au, the water loss rate stagnates (lower bound value of 2.4×10^{25} molecules/s at $\approx$ 3.5-3.6 au), also suggesting the

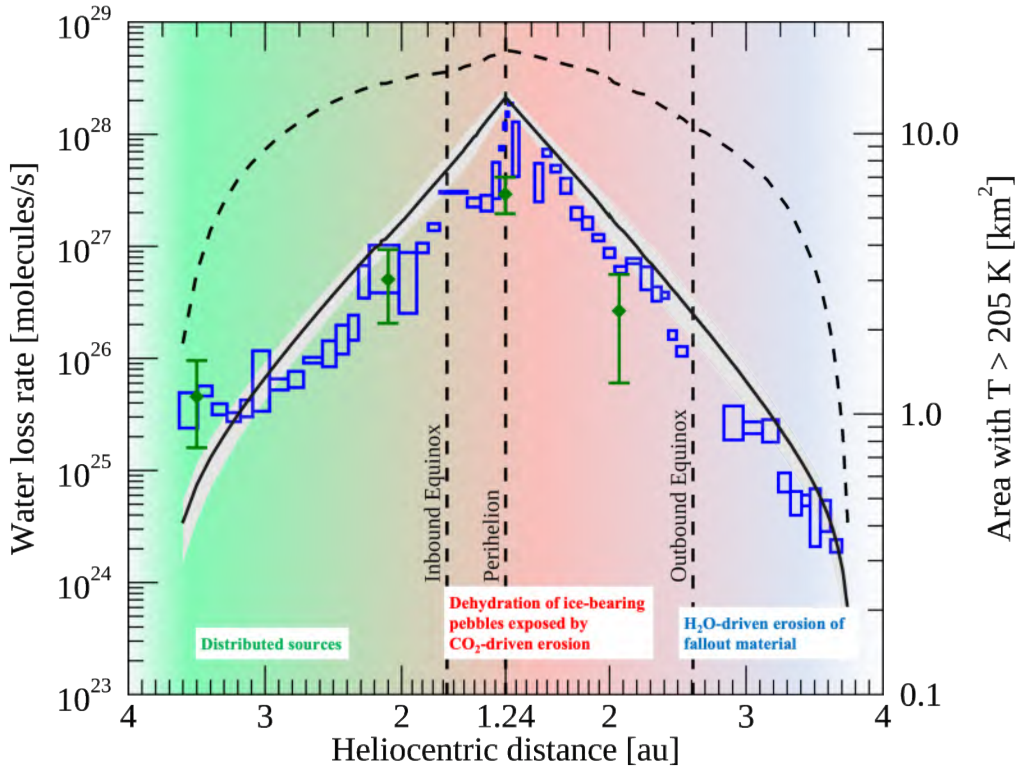

Figure 3. Solid line: computed water vapor loss rate compared with the estimates by the DFMS/COPS observations (blue boxes, Läuter et al. 2020)). The computation has been performed assuming a potentially all active surface, that is all the nucleus surface at $T > 205$ K ejects water. The gray band encompasses the maximum and minimum simulated water loss rate over one comet rotation, while the average value is represented by the black line. The blue boxes account for the uncertainties of the observed loss rate. Green symbols: estimated contribution from distributed sources at selected orbital positions (see Section 6).The different background colors indicate the dominating water production mechanisms at different orbital phases (indicated in the plot) as discussed in detail in Sections 4, 5, and 6. Dashed line: average value of the nucleus area where $T > 205$ K.

occurrence of a local minimum at ≈3.2 au. The comparison of the measured and modeled water loss rate curves (Figs. 3 and 4) indicates that the latter provides a generally good match, in particular for the outbound phase, while somewhat larger discrepancies can be noted for the inbound orbit, and in particular at large heliocentric distances, where the water loss rate is largely underestimated. We point out that the modelled curve stems directly from the application of the model assuming a potentially all active surface. In the following sections, we discuss in greater detail the comparison between the measured and modeled water loss rate for different orbital phases, defining up to what extent the assumption of a potentially all active surface is valid, and the resulting implications on the processes contributing to water production.

4.1 From around perihelion to the outbound equinox

In Fig. 4, we show the ratio between the modeled and measured water loss rate for the best possible match at each position, by taking into account the corresponding variability intervals of the measured and modeled values. Around perihelion, the modeled water loss rate curve overestimates the measured one approximately by a factor two (with the exception of the pre-perihelion phase, where the water loss rate is overestimated by a factor ≈4). According to Ciarniello et al. (2022) and (Fulle 2021), more than 92.5 ± 2.5% of comet 67P/Churyumov-Gerasimenko is composed by pebbles with a relatively low water ice content ($\delta = 50^{+70}_{-25}$, Fulle 2021)[1]. These, having $\delta > \delta_{MAX}$ (so that $D > E$, Fig. 2), cannot sustain water-driven erosion at the computed average temperature of the surface pebbles (T=275 K, Fulle et al. 2020; Fulle 2021) in the southern hemisphere during the polar summer, and are completely dehydrated in about ≈ 25 minutes once exposed (Fulle 2021). As discussed in Section 2 this condition would be consistent with the adopted assumption of a potentially all active surface, only if CO_2-driven erosion is sufficiently fast to mobilize enough chunks and expose enough sub-surface pebbles before complete dehydration occurs (Gundlach et al. 2020, see also Fulle (2021) for details on the resulting surface erosion). As the modelled water loss rate overestimates the measured one around perihelion, we

[1] The dust-to-ice mass ratio in the fraction (92.5 ± 2.5%) of the nucleus of 67P with low water ice content ($\delta = 50^{+70}_{-25}$), determines the dust-to-ice mass ratio of the chunk deposits in the northern hemisphere, and in particular in Hapi. Assuming the deposits are composed of chunks ejected at perihelion from the southern hemisphere (Keller et al. 2017), it can be shown that, upon dehydration, chunks develop an external crust of approximately half of the total volume, thus doubling their final dust-to-ice mass ratio before reaching the northern hemisphere. Cambianica et al. (2020) showed that the dust-to-ice mass ratio of the deposits in Hapi is $\delta_H = 100^{+140}_{-50}$, implying an original value of the chunks at ejection of $\delta = 50^{+70}_{-25}$.

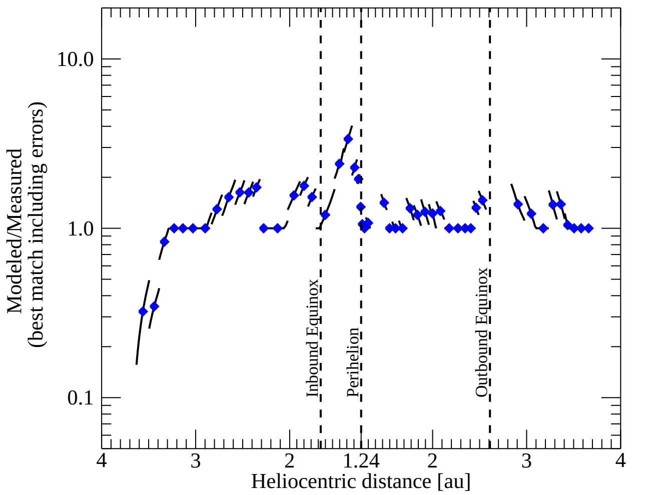

Figure 4. Modeled vs. measured water loss rate ratio. At a given position, if the modeled and measured water loss rate intervals overlap, we assume a value of 1 for the ratio. If not, we compute the model/measured ratio for the closest pair of upper/lower values (best possible match). The blue diamonds indicate the same computation performed only for the central position of the measured water loss rate variability boxes from Läuter et al. (2020).

can conclude that only approximately half of the surface is kept water active, i. e. undergoing CO_2-driven erosion by decimeter-chunk ejection (exposing sub-surface ice-bearing pebbles to dehydration) as suggested by independent modeling of the perihelion activity by Gundlach et al. (2020). Another possible interpretation of our result is that the CO_2-driven erosion rate is 2-4 times slower than the dehydration rate. Thus, even if CO_2 erosion occurs over the whole illuminated surface the active fraction of the nucleus would be reduced down to half-one fourth of the nucleus. However, it is worth mentioning that the estimated water loss rate around perihelion slightly differs among different authors. In this respect, Biver et al. (2019) infer a maximum water loss rate from the Microwave Instrument for the Rosetta Orbiter (MIRO) data ~2.5 times smaller than Läuter et al. (2020)'s, which would imply even a smaller portion of the surface undergoing CO_2-driven erosion and/or slower CO_2-driven erosion rates. Conversely, the peak water production from Combi et al. (2020) (2.8×10^{28} molecules/s) slightly exceeds our maximum value in the same period (2.3×10^{28} molecules/s) thus being more consistent with our original assumption of a potentially all-active nucleus.
Receding from perihelion, along the outbound orbit, the modeled water loss rate tops the measured one, still matching within a factor of 2, at least up to the outbound equinox. This suggests that the progressive reduction of CO_2-driven erosion and freshly exposed sub-surface ice-bearing pebbles, with the comet 67P receding from the Sun, is approximately balanced by the prolongation of the pebble dehydration time.

4.2 Outbound orbit at large heliocentric distance

After the outbound equinox, when the comet was at ≈3.6-3.7 au towards the end of the Rosetta mission, the model provides a close match to the measured water loss rate, suggesting that approximately the whole surface with T>205 K is actually contributing to the observed water production. This is consistent with the activation of fallout deposits, accumulated ubiquitously across 67P surface from the back-fall of material ejected from the southern hemisphere during the polar summer. Fulle et al. (2019) indicate that at least 80% of the ejected chunk's mass slowly falls back on the surface. At 3.6 au, the maximum computed surface temperature would be ≈207 K, implying that even partially dehydrated material with $\delta < \delta_{MAX}(T = 207K) \approx 0.5 \times 10^4$, would be able to sustain water-driven erosion, thus being water-active (fallout self-cleaning, Pajola et al. 2017b) and providing the observed water loss rate. Conversely, at similar heliocentric distances, we expect negligible CO_2-driven erosion (Ciarniello et al. 2022) and consequently a negligible contribution to the water production from freshly exposed sub-surface pebbles. Given this picture, moving along the outbound orbit, from perihelion to relatively large heliocentric distances (≈3.6-3.7 au), we suggest a progressive transition between a CO_2-driven erosion regime, where the water production is provided by the dehydration of freshly exposed sub-surface pebbles, to a H_2O-driven erosion regime, where the dominating contribution is from the activation and self-cleaning of fallout deposits. We also notice that our simulation reproduces the steep decrease of the water loss rate curve outbound, which can be ascribed to the progressive reduction with heliocentric distance of the nucleus surface with $T > 205$ K, i.e. water-active (Fig. 3). This adds up to the flux reduction at larger heliocentric distances due the surface temperature decrease, thereby increasing the steepness of the water loss rate curve.

4.3 Inbound orbit at large heliocentric distance

At $\approx 3.6 - 3.4$ au inbound (August 2014) during the 67P northern summer (Keller et al. 2015), the modeled water loss rate underestimates the measured one at least by a factor 2 (up to ~5 when considering the central position of the water loss rate variability boxes; Figs. 3, 4). As in our computations all the surface elements with T>205 K contribute to the water production, the observed mismatch can be explained by assuming 1) that the predicted modeled surface temperatures underestimate the actual ones in the particular conditions of the northern summer, or 2) that the sublimation of the water-ice fraction of the dust in the coma (distributed sources), not accounted for in our model, provides an additional contribution to water vapour directly coming from the nucleus. We explore both these options separately in sections 5 and 6.

5 SURFACE TEMPERATURES DURING 67P NORTHERN SUMMER IN AUGUST 2014

In August 2014, comet 67P was at $\approx 3.6 - 3.4$ au inbound, during the northern summer (subsolar latitude $\approx 45° - 43°$). As a consequence, the north-facing portion of the nucleus was illuminated, in particular the Hapi region (El-Maarry et al. 2015), located in the comet "neck". Given the concave shape of this region, we may then wonder whether self-illumination effects[2] (Keller et al. 2015), not included in our computation, might account for an additional radiative input, able to increase the local temperature and the resulting water flux. According to previous simulations with different activity models (Keller et al. 2015), the increase in water production during the northern summer at ≈ 3.5 au, when self-illumination effects are included, is of the order of $\approx 10 - 20\%$, thus suggesting that these are not sufficient to explain the resulting mismatch in our computations.

[2] Self-illumination indicates the additional radiative input on a given surface element from reflected visible light and infrared thermal radiation by surrounding areas.

Nonetheless, in the next section we test the effect of self-illumination in the framework of the WEB model, including in our computations the corresponding contribution to the energy input. This allows us to compare the resulting surface temperature distributions with the ones inferred from the infrared thermal emission measured by the Visible InfraRed and Thermal Imaging Spectrometer-Mapper channel (VIRTIS-M) (Coradini et al. 2007) onboard Rosetta, and to evaluate the impact of self-illumination on the computed water loss rate.

5.1 VIRTIS-M measurements for the characterization of the surface temperature distribution in August 2014

From 2 August 2014 to 2 September 2016 (heliocentric distance ranging from 3.62 to 3.44 au, Medium-Term-Planing phase 006: MTP006) the VIRTIS-M IR channel acquired 242 images of comet 67P nucleus, from which it was possible to characterize the surface temperature by modeling the measured thermal emission following the approach of Tosi et al. (2019). With the aim to compare the measured surface temperature distribution with the outcome of our computations, we selected observations imaging as large a fraction of the illuminated nucleus as possible, with the best available spatial resolution. This selection results in six observations (Table 1) acquired with spacecraft-comet distance of around 90 km, and as small a phase angle as possible (≈ 30°).

5.2 Self-illumination contribution and modeled surface temperature distributions in August 2014

In order to evaluate the self-illumination of the nucleus in our simulations, we compute the additional thermal energy input (W m^{-2}) of all the nucleus facets of index j to the facet of index i

$$Z_i = \sum_j \frac{[\overrightarrow{a_i}\overrightarrow{r_{ij}}][\overrightarrow{a_j}\overrightarrow{r_{ij}}]}{4\pi r_{ij}^4} A_j \sigma T_j^4, \quad (2)$$

where $\overrightarrow{r_{ij}}$ is the distance vector between the centers of the facets of index i and j; $\overrightarrow{a_i}$ and $\overrightarrow{a_j}$ are the unit normals for the facets of index i and j, area A_i and A_j, and temperature T_i and T_j; and the square brackets indicate the scalar product operator. Negative values of the scalar products (corresponding to facets not facing each other) and i-j couples with r_{ij} crossing another facet k are not considered in the sum. As Eq. 2 is valid for large values of r_{ij}, while for neighboring facets it produces unphysical results (Davidsson & Rickman 2014), the nearest neighbors of a given facet are excluded from the computation. The term Z_i is summed to the incident solar flux F_i to determine the surface temperature through the relation of Fig. 1. Starting from the base case where self-illumination is not inclued, the term Z_i is applied iteratively to update the surface temperature of all the facets, converging to the final surface temperature distribution after three iterations. We tested our code assuming that the nucleus is a grey-body of emissivity 0.9, and compared our output to similar computations performed with the code adopted in Keller et al. (2015). In particular, we compared the final histogram of the facet temperatures, obtaining a good agreement (see Fig. A1 in Appendix). Notice that with respect to the approach of (Keller et al. 2015), our computation does not account for the additional contribution to self-illumination of the nucleus reflected components. Nonetheless, the good match between the surface temperature histograms obtained with the two different methods indicate that the contribution of the reflected components affect marginally the facet temperature distribution at T>205 K, when the surface can be potentially active.

We then applied the method described above to compute the theoretical surface temperature of each nucleus facet for the illumination conditions (sub-solar latitude and longitude) of VIRTIS images in Table 1. In doing this, we assume that the entire surface is potentially active (thus implying that part of the absorbed energy goes into sublimation of water ice), provided that the corresponding facet surface temperature is larger than 205 K. We note that each VIRTIS image is acquired over approximately 35 minutes, thus each line is in principle characterized by a different sub-solar point position. In practice, the variation of sub-solar latitude is negligible during this time-frame, while the sub-solar longitude varies of about 16.6° due to the comet rotation. Given this, for our simulations we assume the sub-solar longitude value at mid-acquisition. This appears as a reasonable approximation, as we only aim to compare the overall surface temperature distributions from VIRTIS and from our simulations, whereas a pixel-by-pixel comparison is beyond the scope of the present work.
We produce a simulated version of each VIRTIS-M temperature image, by assigning to each VIRTIS-M pixel the maximum temperature among the ones computed for the nucleus facets falling within the pixel. This provides an upper limit of the reference simulated surface temperature of a given pixel, and roughly accounts for the fact that the thermal radiance is dominated by the warmest surface portions within the pixel (Tosi et al. 2019). We limit our analysis only to those pixels (and the surface facets falling within) having VIRTIS-M inferred temperature above T>205 K, being the ones consistent with water emission according to the WEB model. In Figure 5, we show the histograms of the surface temperature distribution for T>205 K, as obtained from the VIRTIS-M observations of Table 1 and the corresponding simulations for a potentially all-active surface. It can be noted that the assumption of a potentially all-active surface, even including self-illumination effects, provides modeled surface temperatures with modal values systematically smaller (up to 8 K) that the measured ones, indicating that this scenario is not compatible with VIRTIS-M observations.

By taking advantage of this set of simulations, we also compute the water flux from the surface for the illumination condition of the 6 VIRTIS-M images of Table 1, to evaluate the additional contribution of self-illumination, with respect to the simulations of Section 3. The resulting water loss rate ranges in the interval ≈0.9-1.6×10^{25} molecules/s. These values, although larger (roughly by a factor two) than the computed water loss rates at similar inbound heliocentric distances without including self-illumination effects, are still significantly smaller than the values measured by ROSINA.

As such, it results that the assumption of a potentially all-active surface, even including self-illumination effects in the proposed model, is not consistent with 1) the measured water loss rate from ROSINA, and 2) with the observed surface temperature distribution measured by VIRTIS-M. In the latter respect, a distribution of surface temperatures more consistent with VIRTIS-M results can be obtained by assuming that a large part of the surface is actually not water-active. In Fig. 5, we show the surface temperature distributions obtained by including self-illumination and assuming that only a small (≈0.4 km^2, namely the smallest area defined by longitude and latitude ranges including the elliptical area of 0.2 km^2 defined by Cambianica et al. 2020) portion of the neck where erosion has been effectively measured by Cambianica et al. (2020) is water active (we refer to this scenario as "active neck"). This scenario leads to larger surface temperatures as on large parts of the surface no incoming energy is spent to sublimate water ice. The modal values of the measured and modeled surface temperature distributions are in agreement typically within 1-3 K, and the root-mean-square deviations are at most

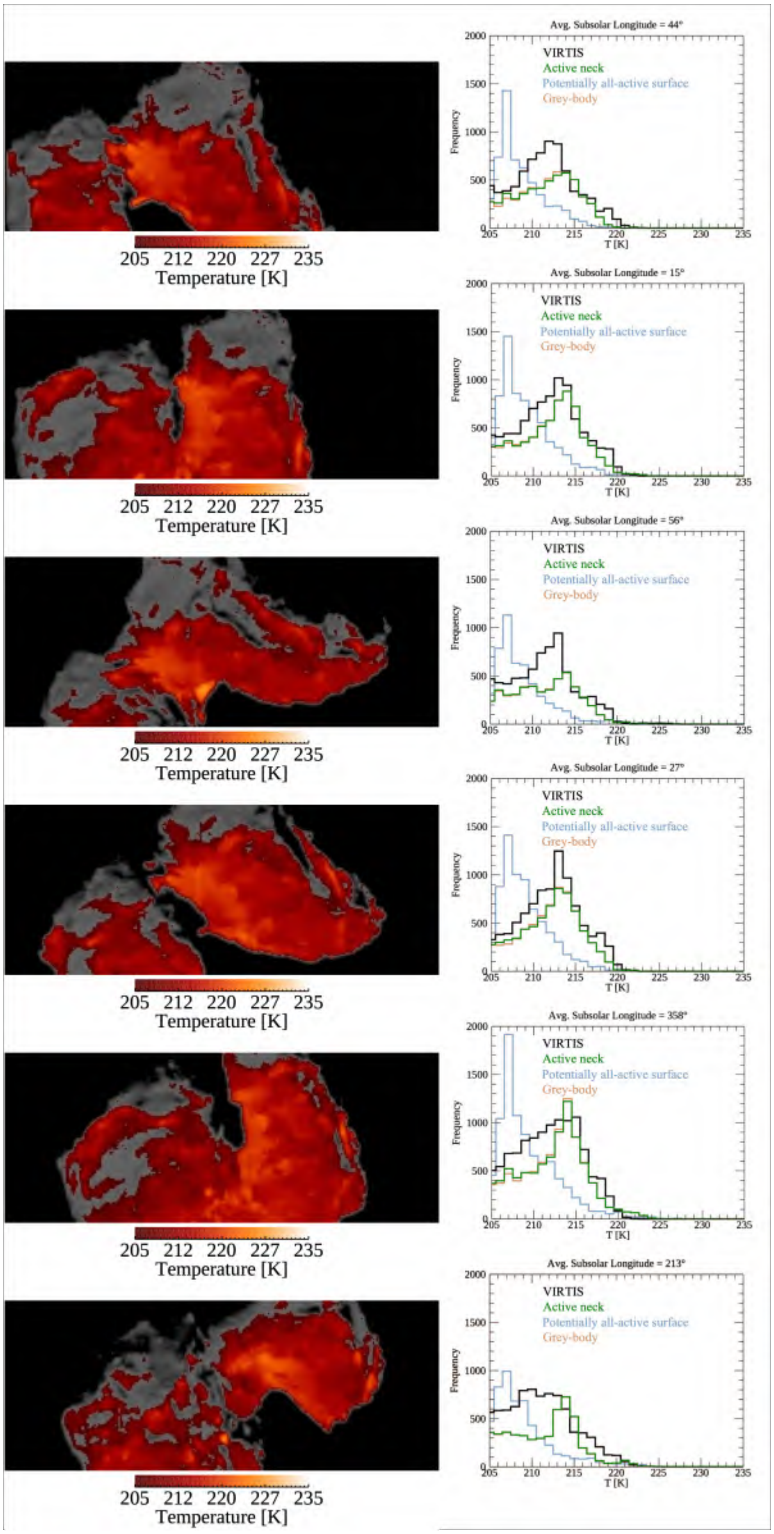

Figure 5. Left panels: 67P temperature images VIRTIS-M-IR observations of table 1. The color bars indicate the surface temperature for pixels with T>205 K, while pixels with T<205 K are shown with grey tones. Black pixels correspond to blank sky or to poorly/not illuminated surface, for which temperature is too low to be estimated. Right panels: surface temperature histogram as obtained from VIRTIS-M temperature images, for pixels with T>205 K (black), and the corresponding histograms obtained by applying the WEB model including self-illumination effects assuming that 1) all the surface is all potentially active (light blue) and 2) only part of neck where surface erosion has been measured ($\approx 0.4\ km^2$, see text) is active (green). For comparison, also the grey-body case with no water sublimation is shown (orange), mostly overlapping the green curve due to the small area of the "active neck" (see text).

Observation ID	Alt. over the surface [km]	Avg. Phase angle [deg]	Sub-solar long. [deg]	Start Time
I1_00366697117.QUB	88.8	28.4	44	2014-08-15T04:19:45.791
I1_00366700717.QUB	88.6	28.2	15	2014-08-15T05:19:45.712
I1_00366740317.QUB	88.5	29.1	56	2014-08-15T16:19:45.686
I1_00366743917.QUB	89.7	29.3	27	2014-08-15T17:19:45.681
I1_00366747517.QUB	89.9	29.6	358	2014-08-15T18:19:45.789
I1_00366765517.QUB	91.8	31.3	213	2014-08-15T23:19:45.774

Table 1. Observational circumstances for the six selected VIRTIS-M-IR observations in MTP006. Each acquisition is composed of 100 lines (from top to bottom in each image of Fig. 5) and each line is composed of 256 samples. The single observation is acquired over approximately 35 minutes, thus corresponding to a variation of the sub-solar longitude of about 16.6° from the top to the bottom line due to comet rotation. Given this, we consider as a reference sub-solar longitude of each image the value at mid-acquisition. For all the observation the heliocentric distance is comprised between 3.54-3.55 au, and the subsolar latitude is 44.1°.

of 4.5 K. In Figs. 5 we also show the comparison of our temperature histograms with those entirely based on a grey body, indicating minor differences with respect to the "active neck" case, given the small extension of the water active area in the latter case. Both these scenarios match very well the measured surface temperature histograms at $T \gtrsim 214$ K. This suggests a limited contribution of surface roughness ($\lesssim$ 10%), as larger amounts would increase the modal temperature and shift the high-temperature tail of the distribution at larger temperature values, inconsistent with observations (see Fig.A2 for a qualitative assessment of the effect of roughness). In some of the cases, the model histograms are significantly lower than observations at 205 K<T$\lesssim$214 K. Such residual differences can be possibly explained by transient diurnal effects depending on the comet rotational phase, not accounted for in the adopted stationary thermophysical model.
The arguments discussed above suggest that a potentially all-active surface is not consistent with the measured surface temperature distributions and cannot explain the water loss rate around 3.5 au inbound, thus indicating that a different process is at work. In Section 6, we discuss the alternative scenario for which the water loss rate in this orbit phase is dominated by distributed sources.

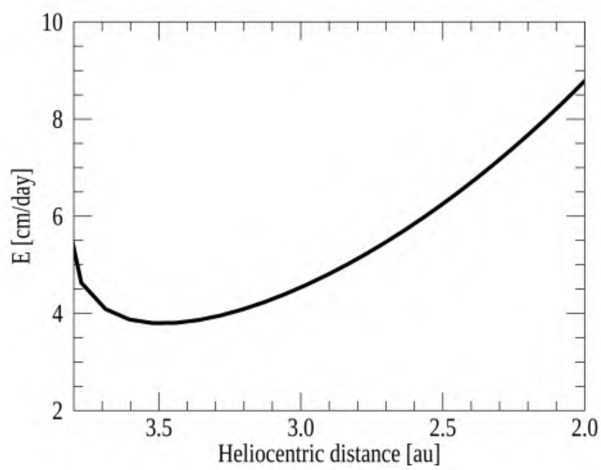

Figure 6. The erosion rate E from Fulle et al. (2020) as a function of heliocentric distance inbound.

6 WATER LOSS RATE FROM DISTRIBUTED SOURCES

Assuming the water active area on 67P at ~3.5 au inbound is mostly limited to the Hapi region, where Cambianica et al. (2020) measured surface erosion, the upper limit on the water loss rate from distributed sources (Q_s) can be straightforwardly computed as (Fulle 2021)

$$Q_s = \frac{E(T) A \rho_d}{\frac{\delta_H}{f} + 1} \qquad f = 1 - \frac{D(T)}{E(T)} \tag{3}$$

where $A \approx 0.4$ km^2 is the water active area undergoing water-driven erosion (Section 5.2), $\rho_d \approx 800$ kg/m^3 is the dust bulk density (Fulle et al. 2017), $\delta_H = 100^{+140}_{-50}$ is the dust-to-ice-ratio in Hapi (Cambianica et al. 2020) and f is the residual water fraction of the dust, which underwent partial dehydration before ejection according to the corresponding ratio of the dehydration and erosion rates. The equation above implies that the entire volatile fraction of the eroded material sublimates within Rosetta orbital distance, which is consistent with the ejection velocity of the emitted dust ($\approx$ 3 m/s) and the dust dehydration time ($\approx 2.3{\times}10^3$ s) yielding a traveled distance of $\approx$ 7 km (see Fulle 2021, and reference therein). However, at least 95% of the distributed sources fall back on the nucleus (Cambianica et al. 2020), so that in average the water production from distributed sources is confined to occur much closer to the nucleus than 7 km. For T=220 K, the characteristic surface temperature in Hapi in August 2014 (Tosi et al. 2019), and accounting for the uncertainty on δ_H, Eq.3 provides $Q_s = 4.4^{+5.0}_{-2.9} \times 10^{25}$ molecules/s, consistent with ROSINA measurements and pointing to a dominant contribution from distributed sources to the water loss rate in August 2014. Interestingly, this interpretation appears also in qualitative agreement with the observed stagnation of the water loss rate when the comet was at $\approx 3.6 - 3.1$ au, given that the erosion rate from Fulle et al. (2020) (although computed neglecting any nucleus self-heating) is characterized by a local minimum within this heliocentric distance interval (Fig. 6), and qualitatively consistent with the reduction of surface erosion in Hapi measured by Cambianica et al. (2020) during 2014. However, we note for completeness that such behavior is not confirmed by MIRO data. In fact, at similar heliocentric distances, Biver et al. (2019) reports a water loss rate of $1.9 - 2.5 \times 10^{25}$ around 3.6 au, monotonically increasing to $3.8 - 5.8 \times 10^{25}$ around 3.2 au. Moving to smaller heliocentric distances inbound, Ciarniello et al. (2022) showed that the blueing of 67P/CG nucleus towards perihelion is provided by the progressive exposure of WEBs as Blue Patches (BPs, water-ice-rich spots with δ =2, brighter and bluer than the average surface) due to CO_2-driven erosion. WEBs can sustain water-driven erosion up to perihelic surface temperatures, thus contributing to distributed sources. The water loss rate from distributed sources originating from the BPs at a given time can be estimated by integrating Eq. 3 across the whole surface having T> 205 K, accounting for the temperature-dependent erosion rate of each facet, assuming the BP dust-to-ice mass ratio, and weighing for the BP fraction on the nucleus. We find that at the heliocentric distance of ≈2.1 au inbound, with BP fraction of 0.28 − 0.87% (Ciarniello et al. 2022) and accounting for the variability of the insolation condition during one comet rotation, the water loss rate from distributed sources originating in the BPs is $\approx 2-9\times10^{26}$ molecules/s, consistent with the measured water loss rate, and indicating a substantial contribution at this orbit phase. Around perihelion (BP fraction ∼ 1.2 − 1.9%, Ciarniello et al. 2022), our computation provides $\approx 2-4\times10^{27}$ molecules/s, significantly smaller than the measured values $Q = [1.1-1.6]\times10^{28}$ molecules/s. This is consistent with the < 15% upper limit on the contribution from distributed sources to the total water loss rate estimated by Biver et al. (2019) at similar heliocentric distances[3], and indicates that the additional contribution from dehydrating pebbles, exposed by the intense CO_2-driven erosion, is required. After perihelion, at ≈ 2.1 au outbound, with BP fraction ≈ 0.08 − 0.52% (Ciarniello et al. 2022) we estimate a water loss rate from distributed sources of $\approx 0.6-5.6\times10^{26}$ molecules/s, smaller than the observed one, and pointing to a dominant contribution from water production occurring directly on the nucleus. Moving at larger heliocentric distances, Ciarniello et al. (2022) indicate a substantial reduction of BP fraction across the nucleus (≈ 0% around 2.7 au), implying negligible contribution from distributed sources.

7 THE CO_2 LOSS RATE

In Ciarniello et al. (2022) it has been shown that the color evolution of comet 67P, characterized by a blueing at perihelion, is connected with the progressive exposure of sub-surface water-ice-enriched blocks, thanks to CO_2-driven erosion of the nucleus into decimeter-sized chunks. The color evolution curve of 67P would be consistent with substantial CO_2-driven erosion starting around February 2015, when the comet was at approximately 2.3 au inbound, and thereon dominating the comet nucleus erosion at least up to perihelion. This appears in agreement with the temporal evolution of the CO_2 loss rate reported in Läuter et al. (2020) (Fig. 7), displaying a surge in the production exactly around February 2015, which would imply also an increase in the surface erosion by chunk-ejection. Before February 2015 the CO_2 production is approximately steady around 10^{25} molecules/s, while after perihelion the production decay with heliocentric distance is less steep than the inbound increase. The timing of the CO_2 production surge and of the corresponding CO_2-driven erosion is qualitatively consistent with the proposed time-frame over which the water loss rate is dominated by dehydration of ice-bearing pebbles exposed by CO_2-driven erosion. Unfortunately, a detailed model of the CO_2-driven activity, following the complex time-dependent approach established by Gundlach et al. (2020), cannot be faced here, because it would need to extend such a model (which in the available implementation assumes a constant perihelion insolation on the constantly sunlit southern hemisphere Gundlach et al. 2020), to the complex thermal regime describing the alternation of day and night. This makes such an approach much more complex than Gundlach et al. (2020) and will be the topic of a future paper. Nonetheless, to support the interpretation of the CO_2 temporal evolution, which, as shown above, affects the water production, we attempt here an empirical modeling of the CO_2 production. In particular, we assume that the gas production inbound is given by a baseline gas production of 10^{25} molecules/s driven by CO_2 sublimation in the nucleus at a constant orbital average temperature, plus an additional insolation-driven term depending on heliocentric distance. This latter is modeled following an empirical approach in which the CO_2 production is linked to the modeled water loss rate with a power-law index, to provide the resulting inboud CO_2 production rate $Q^{in}_{CO_2}(T)$ in the form

$$Q^{in}_{CO_2}(T) = K\left(\frac{Q_{H_2O}(T)}{MAX[Q_{H_2O}(T)]}\right)^{\beta} + 10^{25} molecules/s, \quad (4)$$

with K=1.5×10^{27} molecules/s being the peak production rate. We note that in Ciarniello et al. (2022) a similar approach was adopted to empirically describe the inbound evolution of CO_2-driven erosion, linking it directly to the modeled water-driven erosion by using a power-law index $\alpha = 2$. Here we find that a similar value of the power law index $\beta = 2.2 \pm 0.2$ provides a reasonable match to the measured CO_2 loss rate rate (Fig. 7 and Fig. B1 in appendix) consistent with the surge in CO_2 production at ∼2.3 au and the increase of CO_2-driven erosion inferred by Ciarniello et al. (2022). The ratio between the CO_2-driven (H_2O-driven) erosion $E^{in}_{CO_2}$ ($E^{in}_{H_2O}$) and the CO_2 (H_2O) loss rate $Q^{in}_{CO_2}$ ($Q^{in}_{H_2O}$), can be considered as proxy of the erosion efficiency due to CO_2 (H_2O) sublimation. For water ice $E^{in}_{H_2O}/Q^{in}_{H_2O}$ decreases towards perihelion, as $Q^{in}_{H_2O}$ increases much faster (approximately two orders of magnitude) moving at smaller heliocentric distances then $E^{in}_{H_2O}$ (less than one order of magnitude, Ciarniello et al. 2022). Interestingly, the resulting values of β indicate, from a qualitative point of view, the same trend of the CO_2-driven erosion efficiency, also decreasing with reducing heliocentric distance, although at a faster rate, in fact

$$\frac{E^{in}_{CO_2}}{Q^{in}_{CO_2}} \propto \frac{(E^{in}_{H_2O})^{\alpha=2}}{(Q^{in}_{H_2O})^{\beta=2}}\frac{1}{(Q^{in}_{H_2O})^{0-0.4}} = \left(\frac{E^{in}_{H_2O}}{Q^{in}_{H_2O}}\right)^2\frac{1}{(Q^{in}_{H_2O})^{0-0.4}}$$

with Q_{H_2O} increasing approaching perihelion. This supports the idea that similar principles drive the H_2O and CO_2 activity.

Outbound, the observed evolution of the CO_2 loss rate after perihelion ($Q^{out}_{CO_2}$(T)), characterized by the above-mentioned less steep reduction of the production with heliocentric distance compared to the inbound case, cannot be matched by the former modelization. For the outbound phase, we find that a reasonable fit can be provided by adding a decaying exponential term to the baseline production, resulting inc

$$Q^{out}_{CO_2}(T) = K\exp(-t/\tau) + 10^{25}\text{molecules/s}, \quad (5)$$

with a best-fit τ =70 ±5 days (Fig. 7 and Fig. B1 in appendix).

We interpret the exponential decay of the outbound production as a result of the seasonal heat-wave propagation within the nucleus, providing an outbound CO_2 loss rate overcoming the contribution linked to the water loss rate described by Eq. 4 (Capria et al. 2017).

Around 2.8 au outbound the CO_2 loss rate overcomes the water one when the production is about 5×10^{25} molecules/s. Assuming about half of the comet (∼ 25 km^2) ejecting CO_2, this provides a sublimation rate of 1.8×10^{18} molecules/s/m^2. Computing the sublimation rate as the product of the CO_2 pressure and CO_2 expansion velocity in vacuum, this value corresponds to a CO_2 temperature

[3] In addition, Biver et al. (2019) estimates a < 50% upper limit for distributed sources on November 2015 (r_h ∼ 1.6 au). In the same period Läuter et al. (2020) indicates a total water loss rate of $Q = [3.0-5.3]\times10^{27}$ molecules/s, while Ciarniello et al. (2022) reports a BP fraction of ∼ 0.7 − 1.4%. By simply scaling the perihelic Q_s values to this BP fraction, we obtain a rough estimate of the contribution from distributed sources of the order $\approx 1-3\times10^{27}$ molecules/s. These values, derived by assuming perihelic insolation conditions, overestimate the real ones in November 2015, and are already consistent within error bars with the distributed sources upper limit provided Biver et al. (2019) for the same period.

of 84 K and an intra-pebble pressure of ~40 μPa. Such a low CO_2 pressure, at least a factor 10^4 lower than the water pressure in water active areas (surface temperature T>205 K, P>0.325 Pa), supports the idea that only water vapour ejects sub-cm dust, even if the water loss rate is smaller than the CO_2 one. A proper computation of the CO_2 loss rate taking into account the inter-pebble pressure needs a complete time-dependent approach of the contemporary water and CO_2 sublimation, following Gundlach et al. (2020). For the water case, the ratio between the intra-pebble vs inter-pebble pressures in the first pebble layer can be approximated by the following equation

$$\frac{P_{intra}}{P_{inter}} = 1 + \frac{45}{14}\frac{R}{r}, \qquad (6)$$

derived by combining Eq. 5 and Eq. 16 of Fulle et al. (2020), where R≈ 5 mm is the pebble radius and r≈ 50 nm is the dust monomer radius (Güttler et al. 2019), yielding $R/r \approx 10^5$. This fact points out that the results of water sublimation experiments performed on dust aggregates with $R/r < 10$ (Kossacki et al. 2023) cannot be straightforwardly extrapolated to explore the steep pressure gradients at the surface of pebbles. ~~The CO_2 baseline production of 10^{25} molecules/s would correspond to an internal average orbital temperature of about 80K over half of the surface, assuming free CO_2-ice sublimation at negligible pressure, e.g. at the surface of the pebbles inside the nucleus (inter-pebble). Possible CO_2-ice sublimation inside the pebbles (intra-pebble), would occur at higher temperatures, according to the higher pressure inside each pebble (Fulle et al. 2020), potentially providing an additional contribution to the baseline production. Whereas the free sublimation of inter-pebble CO_2, occurring at negligible pressure, cannot overcome the tensile strength bonding the pebbles to the nucleus driving the ejection of pebble chunks, the high-pressure sublimation of intra-pebble CO_2 might potentially eject chunks. However, this would occur at depths larger than the size of the chunks observed in the 67P coma, suggesting limited intra-pebble CO_2 sublimation negligible contribution to the baseline CO_2 loss rate.~~

Following the same approximate approach as above we obtain a baseline production rate of 10^{25} molecules/s assuming a CO_2 ice temperature of 80 K. An internal average orbital temperature of about 80 K may characterize the southern hemisphere only, where most CO_2 loss has been observed. The internal average orbital temperature of the northern hemisphere is probably much lower, consistent with the much lower total insolation there, with the CO loss rate independent of the CO_2 one (Läuter et al. 2019), and with the similar absolute values of the CO and CO_2 loss rates, requiring an internal average orbital temperature of about 30 K only where most CO-ice (much more volatile than CO_2-ice) is sublimating. Attree et al. (2023) have shown that the here proposed water loss rate model provides the best fit of the radial non-gravitational nucleus acceleration when compared to other available models of the water loss rate. They may further improve the fits of the other non-gravitational accelerations, torques, and nucleus spin motion implementing the here proposed model of the CO_2 loss rate.

8 CONCLUSIONS

We modeled the water loss rate of comet 67P/Churyumov-Gerasimenko as inferred from the COPS and DFMS sensors of the ROSINA experiment (Läuter et al. 2020) throughout the escort phase of the Rosetta mission, by adopting the WEB model (Fulle et al. 2020; Ciarniello et al. 2022). The main conclusions of this study can be summarized as follows:

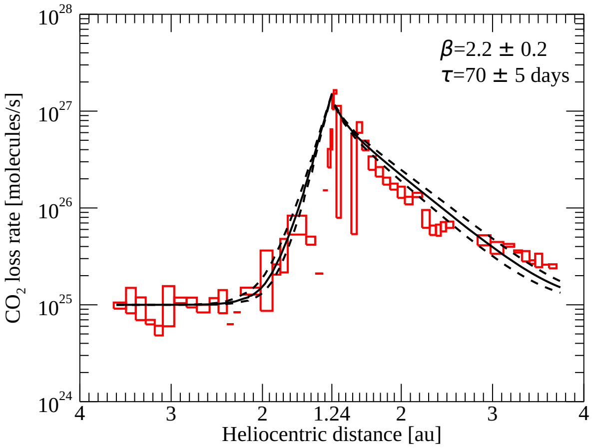

Figure 7. Empirical best-fit (solid black line) of the CO_2 production rate from (Läuter et al. 2020) (red boxes). Dashed lines correspond to the upper and lower bounds of β and τ.

(i) At perihelion, water production mostly arises from the dehydration of water-poor pebbles, continuously exposed by the intense CO_2-driven erosion (Gundlach et al. 2020) involving part of the illuminated nucleus. This is consistent with the observed evolution of CO_2 production, for which we present an empirical modelization.

(ii) At larger heliocentric distances outbound, fallout deposits widespread across the entire nucleus progressively activate (self-cleaning defined by Pajola et al. 2017b), providing a dominating contribution to the water loss rate.

(iii) The observed steep decrease of the water production with increasing heliocentric distance outbound is predicted by the proposed model as resulting from the progressive reduction of the nucleus area with $T > 205$ K. In this respect, this work improves the results from previous studies (Skorov et al. 2020; Davidsson et al. 2022) where such dependence has been linked to the presence of a dust mantle with variable thickness.

(iv) During the inbound phase the water loss rate at large heliocentric distances (3.6 - 3.4 au) is dominated by distributed sources, originating in the active neck. This is consistent with the analysis of the surface temperature distribution as inferred from VIRTIS data (Tosi et al. 2019), suggesting that most of the nucleus is not water-active.

(v) The contribution from distributed sources originating in the BPs (Ciarniello et al. 2022) can explain the measured water loss rate approximately up to the inbound equinox.

(vi) The observed inbound-outbound asymmetry of the water loss rate curve is consistent with the water production being dominated by distributed sources at large inbound heliocentric distances and nucleus fallout self-cleaning at large outbound heliocentric distances.

(vii) Our good fit of the measured nucleus temperatures in the range $214 \lesssim T \lesssim 225$ K suggests a low roughness of the nucleus surface.

ACKNOWLEDGEMENTS

We thank an anonymous reviewer for helpful comments and suggestions which improved the paper. Part of this research was supported by the ESA Express Procurement (EXPRO) RFP for IPL-PSS/JD/190.2016 and by the Italian Space Agency (ASI) within the ASI-INAF agreements I/032/05/0 and I/024/12/0. This work made use of the illumination maps of Beth et al. (2017), available through the Virtual European Solar and Planetary Access (VESPA) (http://vespa.obspm.fr/) with the support of CDPP (http://www.cdpp.eu)

DATA AVAILABILITY

The VIRTIS calibrated data are publicly available through the European Space Agency's Planetary Science Archive website (`https://archives.esac.esa.int/psa/`).

REFERENCES

Altwegg K., et al., 2015, Science, 347, 1261952

Attree N., Jorda L., Groussin O., Agarwal J., Lasagni Manghi R., Tortora P., Zannoni M., Marschall R., 2023, A&A, 670, A170

Balsiger H., et al., 2007, Space Science Reviews, 128, 745

Beth A., et al., 2017, in European Planetary Science Congress. pp EPSC2017–634

Biver N., et al., 2019, A&A, 630, A19

Blum J., et al., 2017, Monthly Notices of the Royal Astronomical Society, 469, S755

Bouziani N., Jewitt D., 2022, ApJ, 924, 37

Brownlee D., et al., 2006, Science, 314, 1711

Cambianica P., et al., 2020, Astronomy and Astrophysics, 636, A91

Capria M. T., et al., 2017, Monthly Notices of the Royal Astronomical Society, 469, S685

Ciarniello M., et al., 2022, Nature Astronomy, 6, 546

Combi M., et al., 2020, Icarus, 335, 113421

Coradini A., et al., 2007, Space Sci. Rev., 128, 529

Davidsson B. J. R., Rickman H., 2014, Icarus, 243, 58

Davidsson B. J. R., Samarasinha N. H., Farnocchia D., Gutiérrez P. J., 2022, MNRAS, 509, 3065

Delsemme A., 1982, in , Comets. Univ. of Arizona Press Tucson, pp 85–130

El-Maarry M. R., et al., 2015, Astronomy and Astrophysics, 583, A26

Fulle M., 2021, MNRAS, 505, 3107

Fulle M., et al., 2016, Monthly Notices of the Royal Astronomical Society, 462, S132

Fulle M., et al., 2017, MNRAS, 469, S45

Fulle M., et al., 2019, Monthly Notices of the Royal Astronomical Society, 482, 3326

Fulle M., Blum J., Rotundi A., Gundlach B., Güttler C., Zakharov V., 2020, Monthly Notices of the Royal Astronomical Society, 493, 4039

Gundlach B., Blum J., Keller H. U., Skorov Y. V., 2015, A&A, 583, A12

Gundlach B., Fulle M., Blum J., 2020, Monthly Notices of the Royal Astronomical Society, 493, 3690

Güttler C., et al., 2019, Astronomy and Astrophysics, 630, A24

Hansen K. C., et al., 2016, Monthly Notices of the Royal Astronomical Society, 462, S491

Hu X., et al., 2017, Astronomy and Astrophysics, 604, A114

Keller H. U., et al., 2015, Astronomy and Astrophysics, 583, A34

Keller H. U., et al., 2017, Monthly Notices of the Royal Astronomical Society, 469, S357

Kelley M. S. P., Lindler D. J., Bodewits D., A'Hearn M. F., Lisse C. M., Kolokolova L., Kissel J., Hermalyn B., 2015, Icarus, 262, 187

Kossacki K. J., Wesołowski M., Szutowicz S., Mikołajków T., 2023, Icarus, 398, 115518

Läuter M., Kramer T., Rubin M., Altwegg K., 2019, MNRAS, 483, 852

Läuter M., Kramer T., Rubin M., Altwegg K., 2020, MNRAS, 498, 3995

Lemos P., Agarwal J., Schröter M., 2023, MNRAS, 519, 5775

Lis D. C., et al., 2019, A&A, 625, L5

Müller D. R., et al., 2022, A&A, 662, A69

O'Rourke L., et al., 2020, Nature, 586, 697

Ott T., et al., 2017, Monthly Notices of the Royal Astronomical Society, 469, S276

Pajola M., et al., 2017a, Nature Astronomy, 1, 0092

Pajola M., et al., 2017b, Monthly Notices of the Royal Astronomical Society, 469, S636

Pätzold M., et al., 2019, Monthly Notices of the Royal Astronomical Society, 483, 2337

Preusker F., et al., 2015, Astronomy and Astrophysics, 583, A33

Skorov Y., Blum J., 2012, Icarus, 221, 1

Skorov Y., Keller H. U., Mottola S., Hartogh P., 2020, MNRAS, 494, 3310

Tosi F., et al., 2019, Nature Astronomy, 3, 649

de Laeter J. R., Böhlke J. K., Bièvre P. D., Hidaka H., Peiser H. S., Rosman K. J. R., Taylor P. D. P., 2003, Pure and Applied Chemistry, 75, 683

APPENDIX A: SURFACE TEMPERATURE HISTOGRAMS FROM GREY BODY MODELS

APPENDIX B: CO_2 PRODUCTION RATE EMPIRICAL MODELS

This paper has been typeset from a TEX/LATEX file prepared by the author.

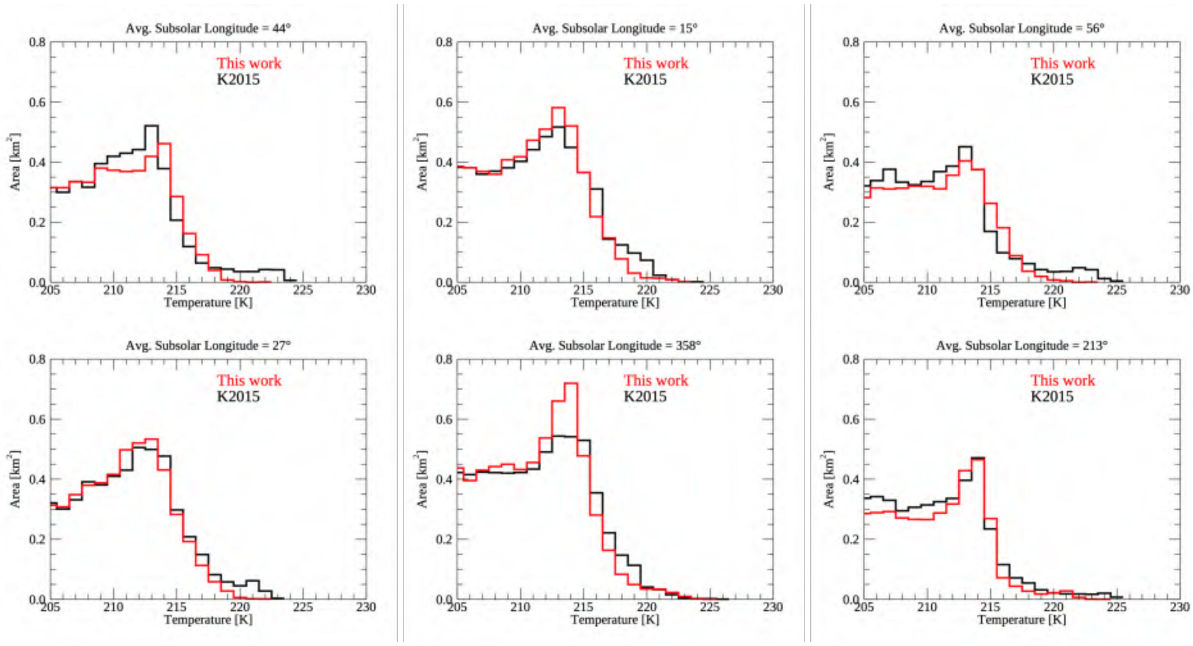

Figure A1. Comparison of the facet temperature histograms at T>205 K for the grey body case computed with our code (red) and the one employed for thermophysical modeling in Keller et al. (2015) (K2015, black). For each facet, the corresponding area is taken into account. The different panels correspond to the reference illumination conditions (subsolar point and heliocentric distance) of the VIRTIS-M-IR observations of Table 1.

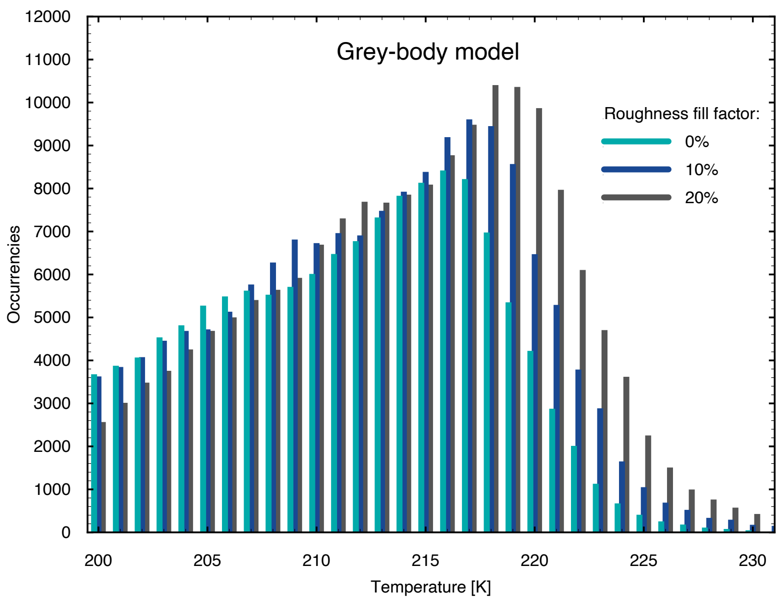

Figure A2. Surface temperature histograms, assuming a grey-body model (Keller et al. 2015), for different levels of roughness. The roughness is modeled in terms of the fraction of surface covered in mini-concavities (roughness fill factor), following the approach described in Tosi et al. (2019) for the epoch JD2456892.00288 ($r_h \approx 3.5$ au, inbound), and using the shape model SPG-SHAP7 v1.6 (Preusker et al. 2015) decimated to about 300,000 facets. The increase of the roughness fill factor yields to a progressively larger modal temperature and a larger high-temperature tail in the histograms.

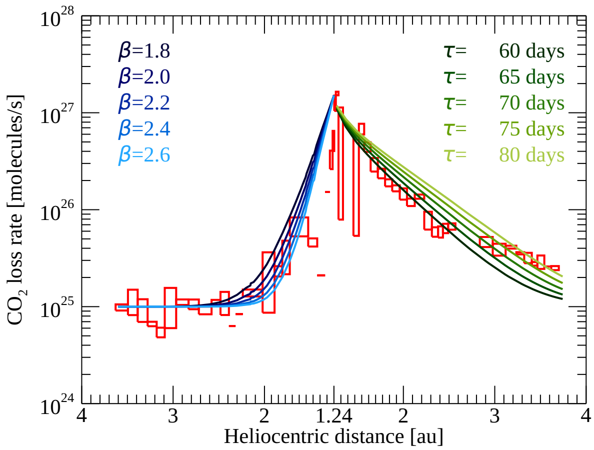

Figure B1. Empirical models (coloured lines) of the CO_2 production rate from (Läuter et al. 2020) (red boxes) for different values of β and τ.